Ambipolar field effect in the ternary topological insulator $(Bi_xSb_{1-x})_2Te_3$ by composition tuning

Desheng Kong[1†], Yulin Chen[2,3,4†], Judy J. Cha[1], Qianfan Zhang[1], James G. Analytis[2,4], Keji Lai[2,3], Zhongkai Liu[2,3,4], Seung Sae Hong[2], Kristie J. Koski[1], Sung-Kwan Mo[5], Zahid Hussain[5], Ian R. Fisher[2,4], Zhi-Xun Shen[2,3,4] and Yi Cui[1,4]*

Topological insulators exhibit a bulk energy gap and spin-polarized surface states that lead to unique electronic properties[1-9], with potential applications in spintronics and quantum information processing. However, transport measurements have typically been dominated by residual bulk charge carriers originating from crystal defects or environmental doping[10-12], and these mask the contribution of surface carriers to charge transport in these materials. Controlling bulk carriers in current topological insulator materials, such as the binary sesquichalcogenides Bi_2Te_3, Sb_2Te_3 and Bi_2Se_3, has been explored extensively by means of material doping[8,9,11] and electrical gating[13-16], but limited progress has been made to achieve nanostructures with low bulk conductivity for electronic device applications. Here we demonstrate that the ternary sesquichalcogenide $(Bi_xSb_{1-x})_2Te_3$ is a tunable topological insulator system. By tuning the ratio of bismuth to antimony, we are able to reduce the bulk carrier density by over two orders of magnitude, while maintaining the topological insulator properties. As a result, we observe a clear ambipolar gating effect in $(Bi_xSb_{1-x})_2Te_3$ nanoplate field-effect transistor devices, similar to that observed in graphene field-effect transistor devices[17]. The manipulation of carrier type and density in topological insulator nanostructures demonstrated here paves the way for the implementation of topological insulators in nanoelectronics and spintronics.

The binary sesquichalcogenides Bi_2Te_3, Sb_2Te_3 and Bi_2Se_3 have recently been identified as three-dimensional topological insulators with robust surface states consisting of a single Dirac cone in the band spectra[6-8]. In these materials, topological surface states have been experimentally confirmed using surface-sensitive probes such as angle-resolved photoemission spectroscopy (ARPES)[7,8,18] and scanning tunnelling microscopy/spectroscopy (STM/STS)[19,20]. Several recent magnetotransport experiments have also revealed charge carriers originating from surface states[11,21-23]. However, despite substantial efforts in relation to material doping[8,9,11] and electric gating[13-16], manipulating and suppressing the bulk carriers of these materials, especially in nanostructures, is still challenging because of the impurities formed during synthesis as well as extrinsic doping from exposure to the ambient environment[10-12].

Here, we propose ternary sesquichalcogenide $(Bi_xSb_{1-x})_2Te_3$ as a tunable three-dimensional topological insulator system in which we are able to engineer the bulk properties by means of the bismuth/antimony composition ratio. $(Bi_xSb_{1-x})_2Te_3$ is a non-stoichiometric alloy that has a similar tetradymite structure to its parent compounds Bi_2Te_3 and Sb_2Te_3 (Fig. 1a). To verify the topological nature of $(Bi_xSb_{1-x})_2Te_3$, we performed ARPES measurements on the (0001) plane of $(Bi_xSb_{1-x})_2Te_3$ bulk single crystals with a variety of compositions, yielding experimental Fermi surface topology maps and band dispersions (Fig. 1b). Together with the broad electronic spectra originating from the bulk states, the single Dirac cone that forms the topological surface state band (SSB) is revealed around the Γ point for all ternary compositions, indicated by the hexagram Fermi surfaces (top row) and the sharp linear dispersion in the band spectra (bottom row). The parent compounds, as-grown Bi_2Te_3 (n type) and Sb_2Te_3 (p type), are highly metallic, with the Fermi energy E_F located deep inside the bulk conduction band (BCB) and bulk valence band (BVB), respectively, due to excessive carriers arising from crystal defects and vacancies[8]. With increasing antimony concentration, E_F systematically shifts downward (Fig. 1b, bottom row). In particular, at a bismuth/antimony ratio of 1:1, that is, $(Bi_{0.50}Sb_{0.50})_2Te_3$, the bulk states completely disappear at E_F with a vanished bulk pocket in the Fermi surface map and band dispersion. The surface Dirac cone of $(Bi_xSb_{1-x})_2Te_3$ (Fig. 1c) noticeably exhibits clear hexagonal warping, similar to that of pure Bi_2Te_3 (refs 8,19,24).

The experimentally observed ARPES measurements are qualitatively reproduced by *ab initio* band structure calculations (Fig. 1d) in which the linear SSB dispersion around the Γ point in all compositions confirms their topological non-triviality. This is not surprising, because the spin–orbit coupling strength (critical for the formation of topological insualtors[1-3]) and the bulk energy gap in ternary $(Bi_xSb_{1-x})_2Te_3$, with varying bismuth/antimony ratios, are comparable to those of the parent compounds Bi_2Te_3 and Sb_2Te_3. Consequently, a quantum phase transition to an ordinary insulator does not occur when varying the bismuth/antimony ratios, which is complementary to a recent study on the topological trivial/non-trivial phase transition in the $BiTl(S_{1-\delta}Se_\delta)_2$ system[25]. This non-triviality across the entire compositional range in ternary $(Bi_xSb_{1-x})_2Te_3$ compounds demonstrates a rich material assemblage of topological insulators based on an alloy approach, which is an attractive avenue to search for material candidates with improved properties.

The compositional engineering of the bulk properties of topological insulators can also be applied to nanostructures. Single-crystalline $(Bi_xSb_{1-x})_2Te_3$ nanoplates were synthesized using a catalyst-free vapour–solid growth method using a mixture of Bi_2Te_3 and Sb_2Te_3 powders as precursors. The growth method was established in our previous work[26]. Figure 2a shows a typical optical microscopy image of as-grown $(Bi_xSb_{1-x})_2Te_3$ nanoplates on an oxidized silicon substrate (300 nm SiO_2/silicon) with thicknesses of a few
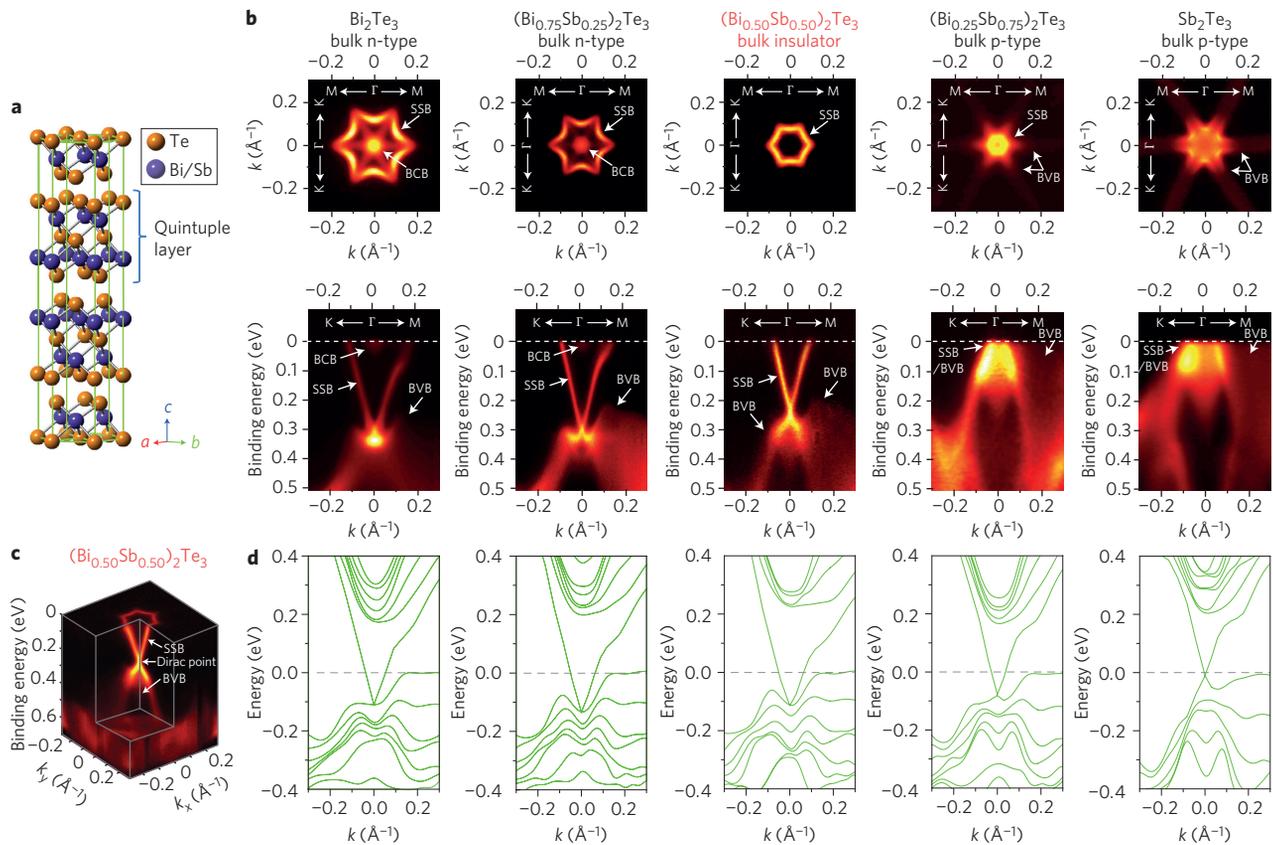
Figure 1 | $(Bi_xSb_{1-x})_2Te_3$, a tunable topological insulator system with a single Dirac cone of surface states. a, Tetradymitetype-type crystal structure of $(Bi_xSb_{1-x})_2Te_3$ consists of quintuple layers (thickness, ~1 nm) bonded by van der Waals interactions. **b**, ARPES Fermi surface maps (top row) and band dispersions along K-Γ-M (bottom row) directions for bulk single crystals with nominal compositions of Bi_2Te_3, $(Bi_{0.75}Sb_{0.25})_2Te_3$, $(Bi_{0.50}Sb_{0.50})_2Te_3$, $(Bi_{0.25}Sb_{0.75})_2Te_3$ and Sb_2Te_3. By increasing the concentration of antimony, E_F exhibits a systematic downshift from the BCB to the BVB through a bulk insulating state achieved in $(Bi_{0.5}Sb_{0.5})_2Te_3$. The SSB consists of a single Dirac cone around the Γ point, forming a hexagram Fermi surface (top row) and V-shaped dispersion in the band structure (bottom row). The apex of the V-shaped dispersion is the Dirac point. Note that the shape of the Dirac cone (especially the geometry below the Dirac point, which hybridizes with the BVB) also varies with bismuth/antimony composition. For a bismuth:antimony ratio less than 50:50, as-grown materials become p-type; E_F resides below the Dirac point, so only the lower part of the Dirac cone is revealed in the ARPES measurement (and the V-shaped dispersion inside the bulk gap is not seen). The n-type SSB pocket on the Fermi surface shrinks with increasing antimony concentration and eventually becomes a p-type pocket hybridized with the bulk band (BVB) in bismuth:antimony concentrations of 25:75 and 0:100. **c**, Three-dimensional illustration of the band structure of $(Bi_{0.50}Sb_{0.50})_2Te_3$ with vanished bulk states on the Fermi surface. SSB forms a single Dirac cone with hexagram Fermi surface. **d**, Ab initio band structure calculations of Bi_2Te_3, $(Bi_{0.75}Sb_{0.25})_2Te_3$, $(Bi_{0.50}Sb_{0.50})_2Te_3$, $(Bi_{0.25}Sb_{0.75})_2Te_3$ and Sb_2Te_3 show qualitative agreement with ARPES measurements (**b**, bottom row), with gapless SSB consist of linear dispersions spanning the bulk gap observed in all the compositions. The difference in E_F between calculated and measured band structures reflects the carriers arising from defects and vacancies in the crystals.

nanometres and lateral dimensions on the scale of micrometres. On these substrates, thin layers of nanoplates are semi-transparent and can be readily identified, with thickness-dependent colour and contrast[26] resembling the optical properties of graphene. The single-crystalline nature of these nanoplates is revealed by the clear lattice fringes in high-resolution transmission electron microscopy (TEM) images (Fig. 2b) and the sharp selected area electron diffraction (SAED) spot pattern (Fig. 2c). Energy-dispersive X-ray spectroscopy (EDX) elemental mapping reveals bismuth, antimony and tellurium distributed across the entire nanoplate without detectable phase separation (Fig. 2d). Nanoplate elemental composition was calibrated using EDX spectra (Fig. 2e). To reflect the initial growth conditions, the nanoplates were labelled with nominal compositions. We fabricated six-terminal Hall bar devices on thin nanoplates with thicknesses ranging from 5 nm to 10 nm for transport measurements (shown schematically in the inset of Fig. 2f). Figure 2f illustrates the dependence of carrier types and area carrier densities on composition measured by the Hall effect, which is consistent with the trend in bulk crystals.

Binary Bi_2Te_3 (n-doped) and Sb_2Te_3 (p-doped) nanoplates have very high carrier densities of $\sim 1 \times 10^{14}$ cm^{-2}. By adjusting the composition in ternary $(Bi_xSb_{1-x})_2Te_3$ nanoplates, the carrier density systemically drops orders of magnitude, with the lowest density achieved in $(Bi_{0.50}Sb_{0.50})_2Te_3$. In addition to the intrinsic defects formed during synthesis, the carrier concentration in chalcogenide topological insulators is often affected by extrinsic dopants contaminating the sample surfaces as a result of atmospheric exposure[10,11]. For example, we have identified water as an effective n-type dopant that is always present in ambient conditions (Supplementary Fig. S5). A systematic approach to modulating the carrier density is therefore essential for nanostructures to achieve low density, because the extrinsic doping depends on environmental conditions.

The bulk carriers in low-density $(Bi_xSb_{1-x})_2Te_3$ nanoplates can be electrically suppressed with backgate field-effect transistor (FET) devices. In ultrathin nanoplates (~5 nm), the typical dependence of resistance R on gate voltage V_G (Fig. 3a) exhibits a very sharp peak that is ~50 times greater than the resistance at large V_G far
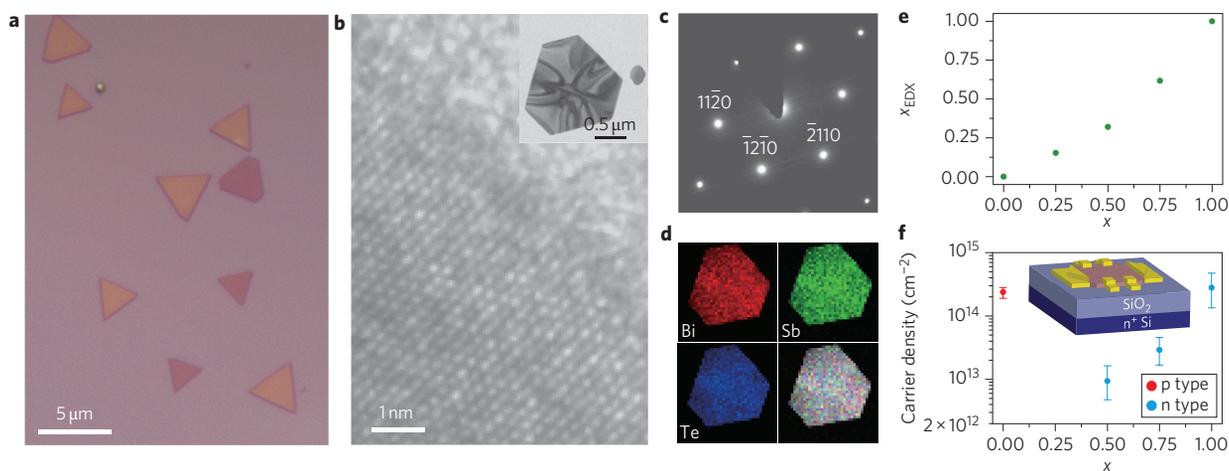
Figure 2 | Characterization of $(Bi_xSb_{1-x})_2Te_3$ nanoplates. a, Optical microscopy image of vapour–solid grown $(Bi_{0.50}Sb_{0.50})_2Te_3$ nanoplates. **b,** High-resolution TEM image of the edge of a $(Bi_{0.50}Sb_{0.50})_2Te_3$ nanoplate (shown in the inset) reveals clear crystalline structure with top and bottom surfaces as (0001) atomic planes. **c,** SAED pattern with sharp diffraction spots indicates that the nanoplate is a high-quality, single crystal. **d,** Bismuth, antimony and tellurium elemental maps obtained from an EDX scan. Overlaying the elemental maps (bottom right panel) reveals the morphology of the nanoplate, indicating that the elements are fairly uniformly distributed without obvious precipitates. **e,** Composition x_{EDX} in $(Bi_xSb_{1-x})_2Te_3$ nanoplates calibrated by EDX spectra. **f,** Nanoplate area carrier density is chemically modulated by adjusting compositions, as determined by the Hall effect. Average carrier concentration from multiple samples is shown as filled circles. Error bars correspond to maximum deviation. Inset: schematic of device structure.

from the peak position. The high-field Hall coefficient R_H reverses its sign when R approaches its maximum value, as shown in Fig. 3b (see Supplementary Fig. S6 for representative Hall traces at different gate voltages). These behaviours resemble the ambipolar field effect observed in graphene[17], which also has two-dimensional Dirac fermions. The gate voltage induces an additional charge density and electrostatically dopes the nanoplate, altering the nanoplate from an n-type conductor to a p-type conductor via a mixed state in which both electrons and holes are present. For regions with only electrons or holes, R and $|R_H|$ decrease with increasing gate-voltage-induced carrier concentration. In the mixed state, R approaches a peak value where the total carrier density is minimized; R_H changes sign when the dominant carrier type (electrons or holes) switches. As expected, no zero-conductance region is observed, presumably due to the presence of surface states inside the bulk bandgap, although other contributions cannot be excluded (Supplementary Figs S8, S9).

The temperature dependence of R further confirms the suppression of bulk conduction in the mixed state. Systematic dependence studies were performed on another device exhibiting the ambipolar field effect (Fig. 4a). In the purely electron-conductive region, the nanoplate shows typical metallic behaviour, with decreasing R as temperature T decreases due to electron–phonon scattering (Fig. 4b). As the nanoplate approaches the mixed state, R begins to increase as T continues to decrease for the entire temperature range (~2–120 K), primarily due to the freeze-out of bulk carriers, also observed in lightly doped topological-insulator Bi_2Se_3 crystals[11]. Note that the actual activation energy E_a cannot be extracted simply by the relation $R \approx R_0 e^{E_a/k_B T}$ (where k_B is the Boltzmann constant) owing to multiple-channel conduction in the presence of surface carriers[23]. Furthermore, the resistance does not diverge at low temperature but gradually saturates to a finite value below 10 K, consistent with metallic surface conduction in parallel with bulk states. Further sweeping V_G to negative values restores the metallic behaviour of the nanoplate as a hole conductor (Fig. 4c).

Finally, a thickness dependence of the transport measurements in FET devices was observed. The suppression of bulk conduction requires the nanoplate to be much thinner than the depletion length D, the length scale controlled by the gate. An order-of-magnitude estimation found by solving the Poisson equation yields $D \approx 11$ nm (Supplementary Fig. S8). For a thicker nanoplate with a thickness of ~9 nm, however, the dependence of R on V_G (Fig. 4d) shows a much weaker tunability than the ultrathin nanoplates, and the entire sample remains n-type, as R_H does not reverse sign. In addition, R decreases with T for all V_G, exhibiting metallic behaviour until ~20 K, below which weak carrier freeze-
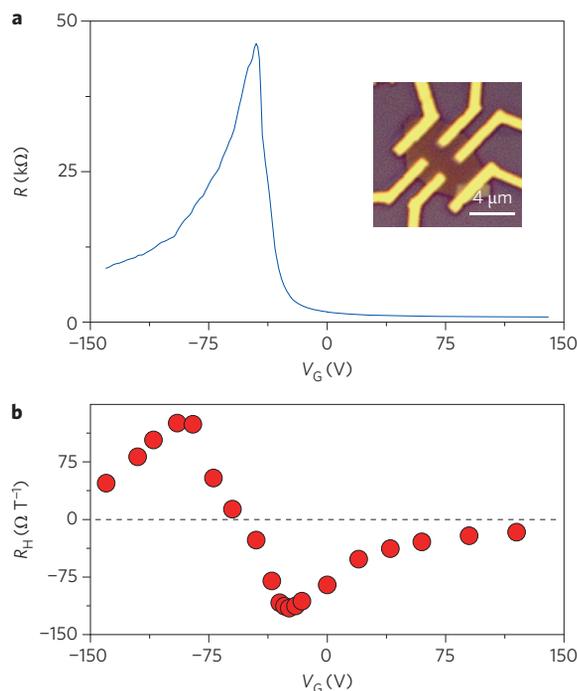

Figure 3 | Ambipolar field effect in ultrathin nanoplates of $(Bi_xSb_{1-x})_2Te_3$. **a,** Typical dependence of resistance R on gate voltage V_G in an ultrathin $(Bi_{0.50}Sb_{0.50})_2Te_3$ nanoplate (thickness, ~5 nm) exhibiting a sharp peak in the resistance and subsequent decay. Inset: optical microscopy image of FET device with a thickness of ~5 nm as determined by AFM. **b,** High-field Hall coefficient R_H versus V_G for the same nanoplate. Each R_H (solid circle) is extracted from the Hall trace for ± 6 T at a certain V_G. At the V_G at peak R, R_H exhibits a reversal in sign.
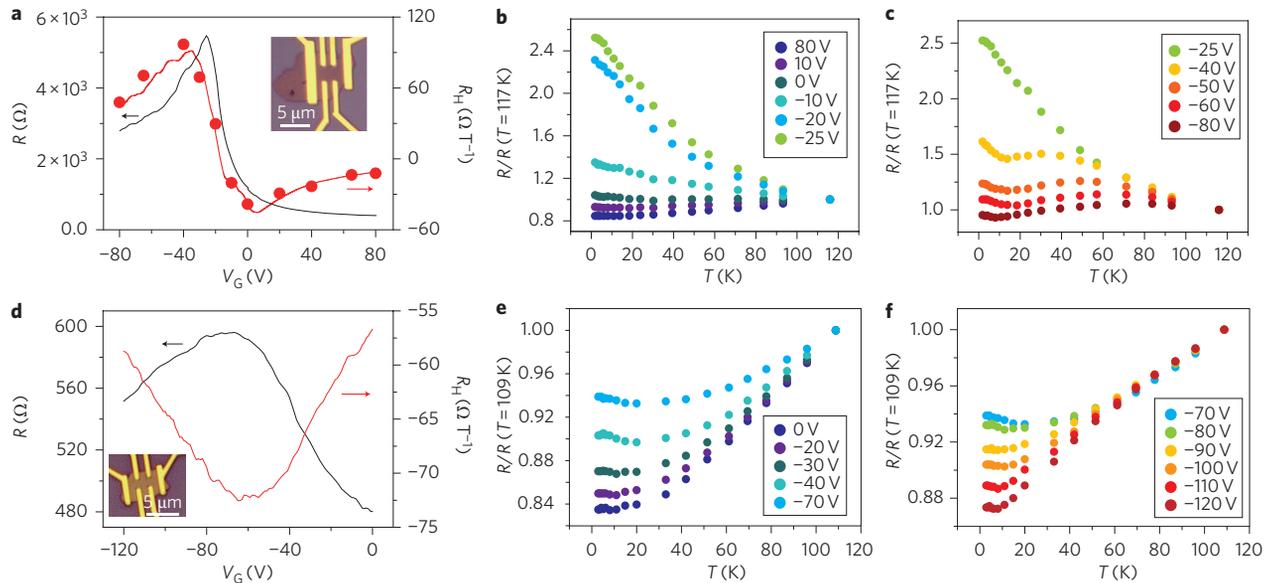
Figure 4 | Temperature-dependent field effect in $(Bi_xSb_{1-x})_2Te_3$ nanoplates. a, Dependence of resistance R and Hall coefficient R_H on gate voltage V_G for a 5-nm-thick $(Bi_{0.50}Sb_{0.50})_2Te_3$ nanoplate (inset), showing the ambipolar field effect. For Hall effect measurements, filled circles indicate high-field Hall coefficient extracted from Hall traces for ±6 T at specific V_G. The curve is obtained by measuring the Hall resistance versus V_G at magnetic fields of ±4 T. **b,c**, Temperature dependence of R at different V_G from electron conductor to mixed state (**b**) and hole conductor to mix state (**c**). R is normalized to its value at the highest measured temperature. **d**, Dependence of resistance R and Hall coefficient R_H on gate voltage V_G for a 9-nm-thick $(Bi_{0.50}Sb_{0.50})_2Te_3$ nanoplate (inset). The Hall coefficient is obtained by measuring the Hall resistance versus V_G at magnetic fields of ±4 T. **e,f**, Temperature dependence of R at different V_G. R is normalized to the value at the highest measured temperature.

out is indicated by a slight rise in R (Fig. 4e,f). Apparently, the nanoplate is too thick to be effectively depleted by gating, and large metallic bulk conduction is always present in the device and contributes to charge transport. It is therefore important to fabricate FET devices from few-layer nanoplates for the effective manipulation of bulk conductivity. Signatures of the ambipolar field effect have been observed previously in several topological insulator nanodevices equipped with backgates[14–16,27]. The observation of the much more pronounced effect reported here benefits from the successful synthesis of ultrathin and low-density nanoplates, made possible by compositional engineering of the bulk carrier density in $(Bi_xSb_{1-x})_2Te_3$ compounds. We note that, in the thinnest limit, the top and bottom surface states may hybridize by quantum tunnelling and open an energy gap, resulting in either a conventional insulator or a two-dimensional quantum spin Hall system[20,28–30]. Gapless SSBs are clearly observed in the *ab initio* band structures on the six-quintuple-layer slab ($\sim$6 nm) shown in Fig. 1d, indicating that the critical thickness of $(Bi_xSb_{1-x})_2Te_3$ compounds enabling the observation of such a transition is thinner than 6 nm. The measured thin nanoplates ($\geq$5 nm) are expected to be beyond the critical thickness[31].

Note that, while we were writing this manuscript, another group also independently identified topological insulator states in $(Bi_xSb_{1-x})_2Te_3$ compounds[31].

Methods

Synthesis. Single crystals of $(Bi_xSb_{1-x})_2Te_3$ were obtained by slow cooling of a ternary melt of varying ratios of bismuth/antimony/tellurium. This mixture was sealed in quartz under a partial pressure of argon. The mixture was heated to 800 °C over 14 h, held at this temperature for an additional 6 h, then cooled over a period of 100 h to 500 °C, then finally cooled naturally to room temperature.

Ultrathin $(Bi_xSb_{1-x})_2Te_3$ nanoplates were grown inside a 12-inch horizontal tube furnace (Lindberg/Blue M) with a 1-inch-diameter quartz tube. A uniform mixture of Bi_2Te_3 and Sb_2Te_3 powders (Alpha Aesar, 99.999%) with a specific molar ratio was placed in the hot centre region as the precursors for evaporation. Degenerately doped silicon substrates with a 300 nm thermally grown oxide film were placed downstream at certain locations, using the temperature gradient along the tube to control the growth temperature. The tube was initially pumped down to a base pressure less than 100 mtorr and flushed with ultrapure argon repeatedly to reduce

residual oxygen. During growth, argon flow provided the impetus to transport the vapour to the substrates. Typical growth conditions of $(Bi_xSb_{1-x})_2Te_3$ nanoplates: powder mixture, $\sim$0.5 g; pressure, 10 torr; carrier gas flow, 15 s.c.c.m.; precursor temperature, 490 °C; duration time, 10 min. $(Bi_xSb_{1-x})_2Te_3$ tended to grow at locations $\sim$12 cm away from the hot centre region, corresponding to a temperature of $\sim$300 °C.

ARPES measurements. ARPES measurements were performed at Beamline 10.0.1 of the Advanced Light Source (ALS) at Lawrence Berkeley National Laboratory. The measurement pressure was kept below 3×10^{-11} torr at all times, and data were acquired by Scienta R4000 analysers at a sample temperature of 10 K. The total convolved energy and angle resolutions were 15 meV and 0.2°, that is, 0.012(1/Å) for photoelectrons excited by 48 eV photons. A fresh surface for ARPES measurement was obtained by cleaving the sample *in situ* along its natural cleavage plane.

Theoretical calculations. First-principle electronic band calculations were performed in a six-quintuple-layer slab geometry using the Vienna *Ab-initio* Simulation Package (VASP). The Perdew–Burke–Ernzerhof type generalized gradient approximation was used to describe the exchange–correlation potential. Spin–orbit coupling was included using scalar-relativistic eigenfunctions as a basis after the initial calculation was converged to self-consistency. A k-grid of $10 \times 10 \times 1$ points was used in the calculations, and the energy cutoff was set to 300 eV. A 2×2 unit cell of randomly substituted bismuth and antimony atoms was used to simulate the structure. The lattice parameters of $(Bi_xSb_{1-x})_2Te_3$ were interpolated from the experimental lattice parameters of Bi_2Te_3 and Sb_2Te_3 according to the composition.

Nanostructure characterizations. Characterization was carried out using optical microscopy (Olympus BX51M, imaged with a $\times100$ objective under normal white illumination), TEM (FEI Tecnai G2 F20 X-Twin microscope, acceleration voltage 200 kV) equipped with an EDX spectrometer, and atomic force microscopy (AFM, Park Systems XE-70). For TEM and EDX characterizations, $(Bi_xSb_{1-x})_2Te_3$ nanoplates were directly grown on 50 nm Si_3N_4 membranes supported by silicon windows. The actual composition of $(Bi_xSb_{1-x})_2Te_3$ nanoplates was calibrated by EDX spectra with Bi_2Te_3 and Sb_2Te_3 spectra as references.

Device fabrication. Backgate FET devices were directly fabricated on as-grown substrates with 300 nm SiO_2 films on silicon. The substrates were first decorated with metal markers based on standard electron-beam lithography followed by thermal evaporation of chromium/gold (5 nm/60 nm). Once a suitable nanoplate was selected, a second patterning step defined multiple chromium/gold (5 nm/100 nm) electrodes using the markers.

Transport measurements. Low-frequency (~200–1,000 Hz) magnetotransport experiments were carried out in an Oxford cryostat with digital lock-in amplifiers (Stanford Research Systems SR830). All transport measurements were measured at a base temperature of 2.0 K unless specified otherwise. A Keithley 2400 source meter was used to apply the gate voltage. The resistance was measured using a standard four-terminal configuration to eliminate contact resistance.

References

1. Moore, J. E. The birth of topological insulators. *Nature* **464,** 194–198 (2010).
2. Hasan, M. Z. & Kane, C. L. Colloquium: topological insulators. *Rev. Mod. Phys.* **82,** 3045–3067 (2010).
3. Qi, X-L. & Zhang, S-C. Topological insulators and superconductors. Preprint at http://arxiv.org/abs/1008.2026 (2010).
4. Bernevig, B. A., Hughes, T. L. & Zhang, S-C. Quantum spin Hall effect and topological phase transition in HgTe quantum wells. *Science* **314,** 1757–1761 (2006).
5. König, M. *et al.* Quantum spin Hall insulator state in HgTe quantum wells. *Science* **318,** 766–770 (2007).
6. Zhang, H. *et al.* Topological insulators in Bi_2Se_3, Bi_2Te_3 and Sb_2Te_3 with a single Dirac cone on the surface. *Nature Phys.* **5,** 438–442 (2009).
7. Xia, Y. *et al.* Observation of a large-gap topological-insulator class with a single Dirac cone on the surface. *Nature Phys.* **5,** 398–402 (2009).
8. Chen, Y. L. *et al.* Experimental realization of a three-dimensional topological insulator, Bi_2Te_3. *Science* **325,** 178–181 (2009).
9. Hsieh, D. *et al.* A tunable topological insulator in the spin helical Dirac transport regime. *Nature* **460,** 1101–1105 (2009).
10. Analytis, J. G. *et al.* Bulk Fermi surface coexistence with Dirac surface state in Bi_2Se_3: a comparison of photoemission and Shubnikov–de Haas measurements. *Phys. Rev. B* **81,** 205407 (2010).
11. Analytis, J. G. *et al.* Two-dimensional surface state in the quantum limit of a topological insulator. *Nature Phys.* **6,** 960–964 (2010).
12. Kong, D. *et al.* Rapid surface oxidation as a source of surface degradation factor for Bi_2Se_3. *ACS Nano* **5,** 4698–4703 (2011).
13. Chen, J. *et al.* Gate-voltage control of chemical potential and weak antilocalization in Bi_2Se_3. *Phys. Rev. Lett.* **105,** 176602 (2010).
14. Checkelsky, J. G., Hor, Y. S., Cava, R. J. & Ong, N. P. Bulk band gap and surface state conduction observed in voltage-tuned crystals of the topological insulator Bi_2Se_3. *Phys. Rev. Lett.* **106,** 196801 (2011).
15. Chen, J. *et al.* Tunable surface conductivity in Bi_2Se_3 revealed in diffusive electron transport. *Phys. Rev. B* **83,** 241304 (2011).
16. Steinberg, H., Gardner, D. R., Lee, Y. S. & Jarillo-Herrero, P. Surface state transport and ambipolar electric field effect in Bi_2Se_3 nanodevices. *Nano Lett.* **10,** 5032–5036 (2010).
17. Novoselov, K. S. *et al.* Electric field effect in atomically thin carbon films. *Science* **306,** 666–669 (2004).
18. Hsieh, D. *et al.* Observation of time-reversal-protected single-Dirac-cone topological-insulator states in Bi_2Te_3 and Sb_2Te_3. *Phys. Rev. Lett.* **103,** 146401 (2009).
19. Alpichshev, Z. *et al.* STM imaging of electronic waves on the surface of Bi_2Te_3: topologically protected surface states and hexagonal warping effects. *Phys. Rev. Lett.* **104,** 016401 (2010).
20. Zhang, Y. *et al.* Crossover of the three-dimensional topological insulator Bi_2Se_3 to the two-dimensional limit. *Nature Phys.* **6,** 584–588 (2010).
21. Peng, H. *et al.* Aharonov–Bohm interference in topological insulator nanoribbons. *Nature Mater.* **9,** 225–229 (2010).
22. Qu, D-X., Hor, Y. S., Xiong, J., Cava, R. J. & Ong, N. P. Quantum oscillations and Hall anomaly of surface states in the topological insulator Bi_2Te_3. *Science* **329,** 821–824 (2010).
23. Xiu, F. *et al.* Manipulating surface states in topological insulator nanoribbons. *Nature Nanotech.* **6,** 216–221 (2011).
24. Fu, L. Hexagonal warping effects in the surface states of the topological insulator Bi_2Te_3. *Phys. Rev. Lett.* **103,** 266801 (2009).
25. Xu, S-Y. *et al.* Topological phase transition and texture inversion in a tunable topological insulator. *Science* **332,** 560–564 (2011).
26. Kong, D. *et al.* Few-layer nanoplates of Bi_2Se_3 and Bi_2Te_3 with highly tunable chemical potential. *Nano Lett.* **10,** 2245–2250 (2010).
27. Kim, D. *et al.* Minimum conductivity and charge inhomogeneity in Bi_2Se_3 in the topological regime. Preprint at http://arxiv.org/abs/1105.1410 (2011).
28. Liu, C-X. *et al.* Oscillatory crossover from two-dimensional to three-dimensional topological insulators. *Phys. Rev. B* **81,** 041307 (2010).
29. Li, Y.Y. *et al.* Intrinsic topological insulator Bi_2Te_3 thin films on Si and their thickness limit. *Adv. Mater.* **22,** 4002–4007 (2010).
30. Cho, S., Butch, N. P., Paglione, J. & Fuhrer, M. S. Insulating behavior in ultrathin bismuth selenide field effect transistors. *Nano Lett.* **11,** 1925–1927 (2011).
31. Zhang, J. *et al.* Dirac band engineering in $(Bi_{1-x}Sb_x)_2Te_3$ ternary topological insulators. Preprint at http://arxiv.org/abs/1106.1755 (2011).

Author contributions

D.K., Y.L.C. and Y.C. conceived the experiments. Y.L.C. and Z.K.L. carried out ARPES measurements. J.G.A. synthesized and characterized bulk single crystals. Q.F.Z. performed electronic structure calculations. D.K. and J.J.C. carried out synthesis, structural characterization and device fabrication for nanoplates. D.K., K.L., J.J.C., S.S.H. and K.J.K. carried out transport measurements and analyses. All authors contributed to the scientific planning and discussions.

Additional information

The authors declare no competing financial interests. Supplementary information accompanies this paper at www.nature.com/naturenanotechnology. Reprints and permission information is available online at http://www.nature.com/reprints. Correspondence and requests for materials should be addressed to Y.C.

Ambipolar field effect in the ternary topological insulator $(Bi_xSb_{1-x})_2Te_3$ by composition tuning

Desheng Kong[+], Yulin Chen[+], Judy J. Cha, Qianfan Zhang, James G. Analytis, Keji Lai, Zhongkai Liu, Seung Sae Hong, Kristie J. Koski, Sung-Kwan Mo, Zahid Hussain, Ian R. Fisher, Zhi-Xun Shen, and Yi Cui

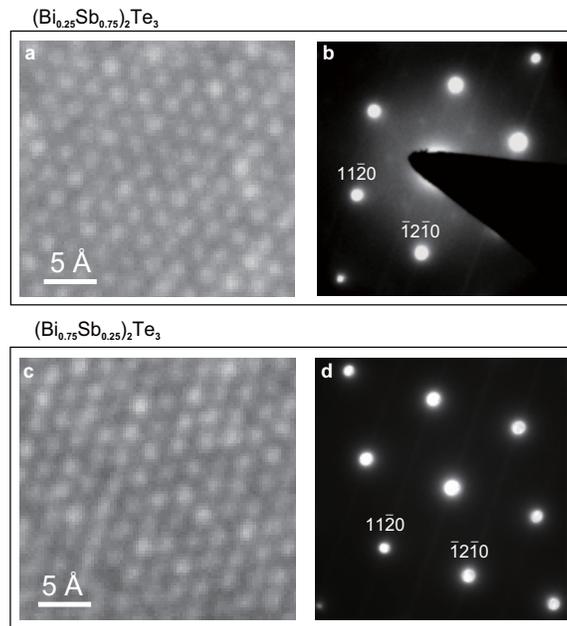[+]These authors contributed equally to this work.
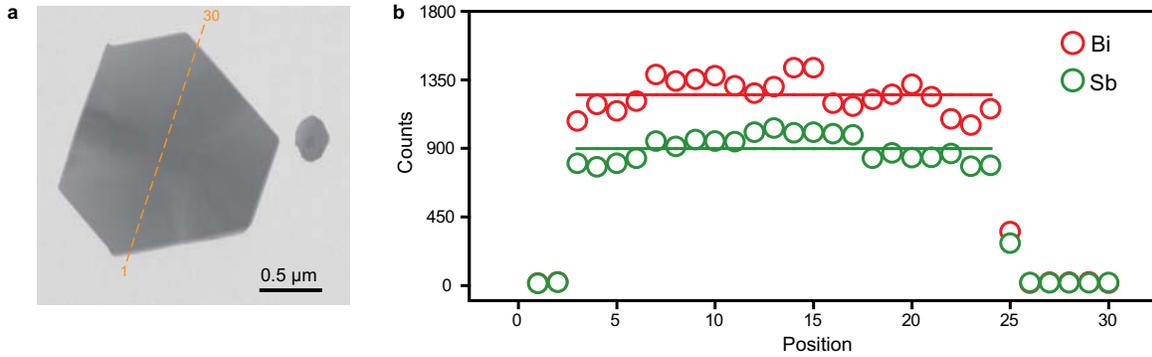
Contents

Figures

- **S1**: Additional structural characterizations on $(Bi_xSb_{1-x})_2Te_3$ nanoplates with different compositions.

- **S2**: Chemical composition analysis of $(Bi_xSb_{1-x})_2Te_3$ nanoplates by STEM-EDX mapping.

- **S3**: Normalized EDX spectra of $(Bi_xSb_{1-x})_2Te_3$ nanoplates with different compositions.

- **S4**: Uniformity of carrier density in $(Bi_xSb_{1-x})_2Te_3$ nanoplates.

- **S5**: Sensitivity of carrier density to H_2O as an environmental dopant.

- **S6**: Hall traces and the approaches to extract the Hall coefficient.

- **S7**: Thickness of the nanoplates measured by atomic force microscopy (AFM).

- **S8**: Band bending due to electrostatic gating with maximum surface depletion length**.**

- **S9**: Carrier concentration of topological surface states in $(Bi_xSb_{1-x})_2Te_3$ system.

Tables

- **S10**: EDX calibration of actual composition in $(Bi_xSb_{1-x})_2Te_3$ nanoplates.

- **S11**: Dependence of area carrier concenration on composition in $(Bi_xSb_{1-x})_2Te_3$

(Bi$_{0.25}$Sb$_{0.75}$)$_2$Te$_3$

(Bi$_{0.75}$Sb$_{0.25}$)$_2$Te$_3$

S1. Additional structural characterizations on (Bi$_x$Sb$_{1-x}$)$_2$Te$_3$ nanoplates with different compositions. a, High resolution TEM image of a (Bi$_{0.25}$Sb$_{0.75}$)$_2$Te$_3$ nanoplate supported on 50 nm-thick SiN$_x$ membrane. **b,** The corresponding selected area electron diffraction (SAED) pattern with sharp diffraction spots. **c,** High resolution TEM image of a (Bi$_{0.75}$Sb$_{0.25}$)$_2$Te$_3$ nanoplate. **d,** The corresponding selected area electron diffraction (SAED) pattern with sharp diffraction spots.
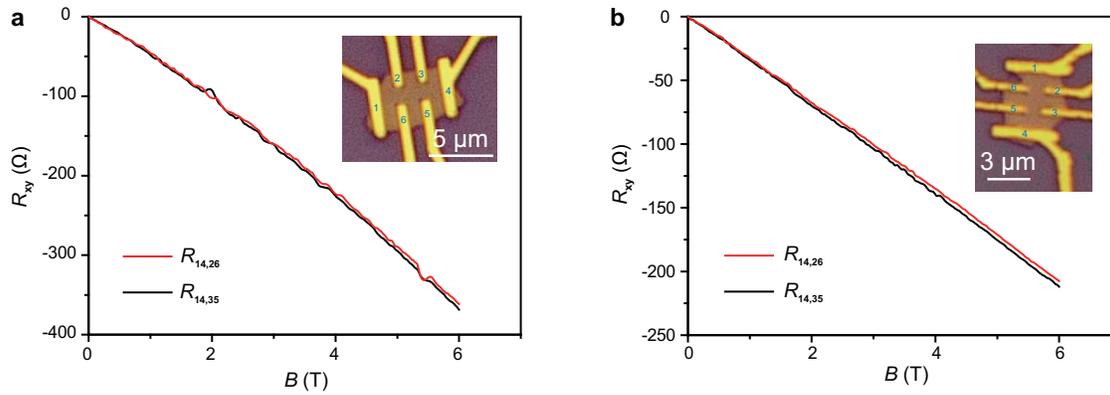
S2. Chemical composition analysis of $(Bi_xSb_{1-x})_2Te_3$ nanoplates by STEM-EDX mapping. a, Scanning transmission electron microscopy (STEM) bright field image of a $(Bi_{0.50}Sb_{0.50})_2Te_3$ nanoplate. EDX spectra are acquired along the orange dash line with spot size less than 1 nm. **b,** Intensity of Bi and Sb peaks reflects the elemental distribution. The solid lines are the averaged counts to guide the eye. The elemental intensity profiles indicates fairly uniform distribution without large precipitates.
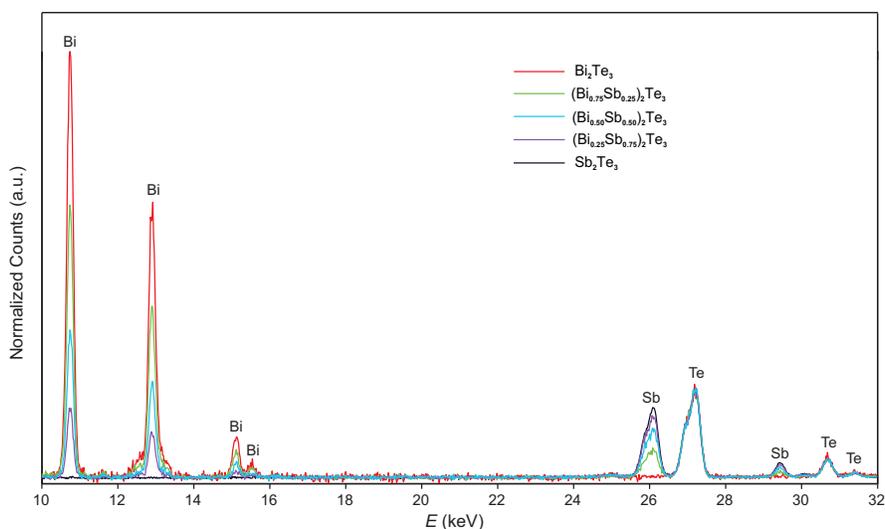
**S3. Normalized EDX spectra of $(Bi_xSb_{1-x})_2Te_3$ nanoplates with different compositions.**
Raw spectra are normalized with respect to Te peaks (27.4 keV) for comparison. Spectra from tenary nanoplates are decomposed to Bi_2Te_3 and Sb_2Te_3 reference spectra to determine the atomic ratio x_{EDX} between Bi and Sb. The results from multiple samples are summarized in Table S10.

a

R_{xy} (Ω): 0, -100, -200, -300, -400

B (T): 0, 2, 4, 6

— $R_{14,26}$
— $R_{14,35}$

5 µm

b

R_{xy} (Ω): 0, -50, -100, -150, -200, -250

B (T): 0, 2, 4, 6

— $R_{14,26}$
— $R_{14,35}$

3 µm

S4. Uniformity of carrier density in (Bi$_x$Sb$_{1-x}$)$_2$Te$_3$ nanoplates. The uniformity of carrier density in the nanoplates is checked by comparing Hall traces from two pairs electrodes. **a,** Hall traces in a (Bi$_{0.50}$Sb$_{0.50}$)$_2$Te$_3$ nanoplate. **b,** Hall traces in a (Bi$_{0.75}$Sb$_{0.25}$)$_2$Te$_3$ nanoplate. The variation of Hall coefficient between two pairs of electrode is within 5%, indicating excellent uniformity in electrical properties. As a result of the lack of stoichiometry, certain inhomogeneity is expected to exists in (Bi$_x$Sb$_{1-x}$)$_2$Te$_3$ alloy system. Such an effect is less severe in nanoplates likely due to the reduced dimension. Note that all the Hall traces are acquired at zero gate voltage.
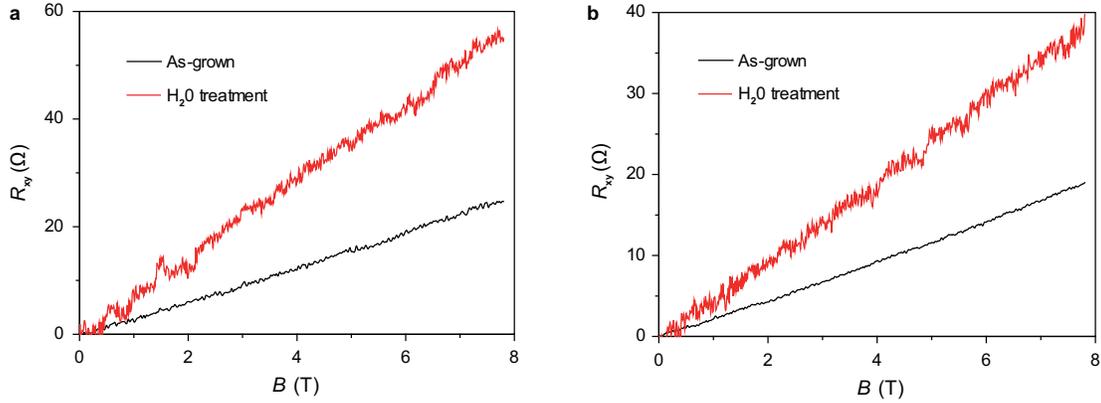
S5. Sensitivity of carrier density to H_2O as an environmental dopant. We have performed control experiments on two p-type Sb_2Te_3 nanoplate devices to study the effect of exposure to H_2O on the carrier concentration. Hall traces from as-grown (black) nanoplates are acquired. Samples are then rinsed in water for 1 min and blew dry. After such a treatment, Hall traces from the same devices are measured again. Apparently, the samples are n-type doped with electrons to compensate the carriers in the hole conductor of Sb_2Te_3 upon water exposure. Large changes in carrier concentrations of $\sim 1 \times 10^{14}$ cm^{-2} are observed for both samples. This effect indicates the transport properties of nanostructured chalcogenide topological insulators are strongly influenced by environmental doping.
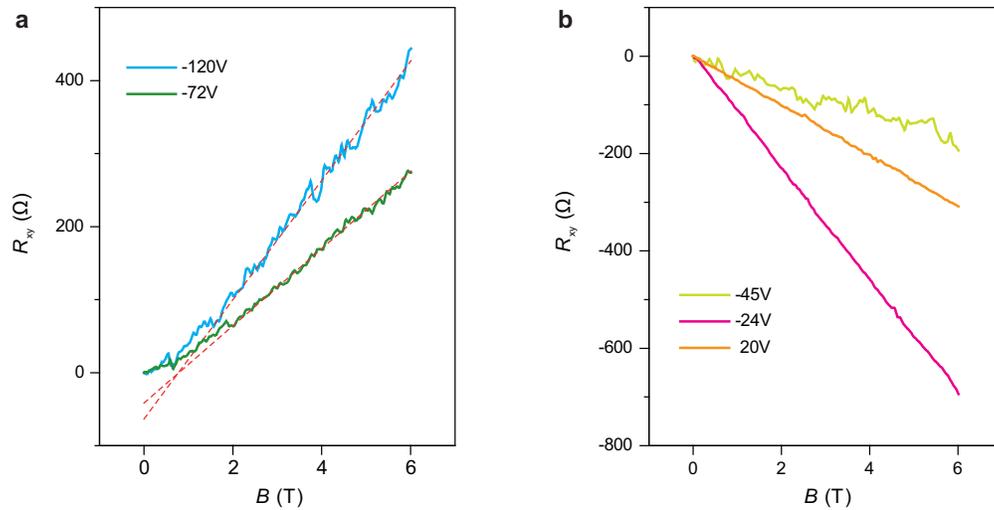
S6. Hall traces and the approaches to extract the Hall coefficient. For the FET device in Fig. 3, representative Hall traces at different gate voltages are shown here. **a,** Hall traces are slightly non-linear at large negative gate voltages presumably due to the presence of multiple carriers. **b,** Hall traces exhibit excellent linearity from relatively small negative gate voltages to positive gate voltages. In the semiclassical transport model, more mobile carriers have larger contribution to low field Hall resistance, whereas the net carrier density determines the Hall traces at high field limit[1]. The high-field Hall coefficient is thus extracted from the linear region of the Hall traces between ~2T and 6T at different gate voltages, as presented in Fig. 3b. Similar approach is used previously to extract the Hall coefficient from non-linear Hall traces[1]. Note that continuous curves of Hall coefficient in Fig. 4a,d are obtained from Hall resistance values at ±4T respectively according to the relation, $R_H = [R_{xy}(4T) – R_{xy}(-4T)] / 8$. The two approaches yield consistent results as shown in Fig. 4a, likely because the measured Hall traces are either very linear or only slightly non-linear.
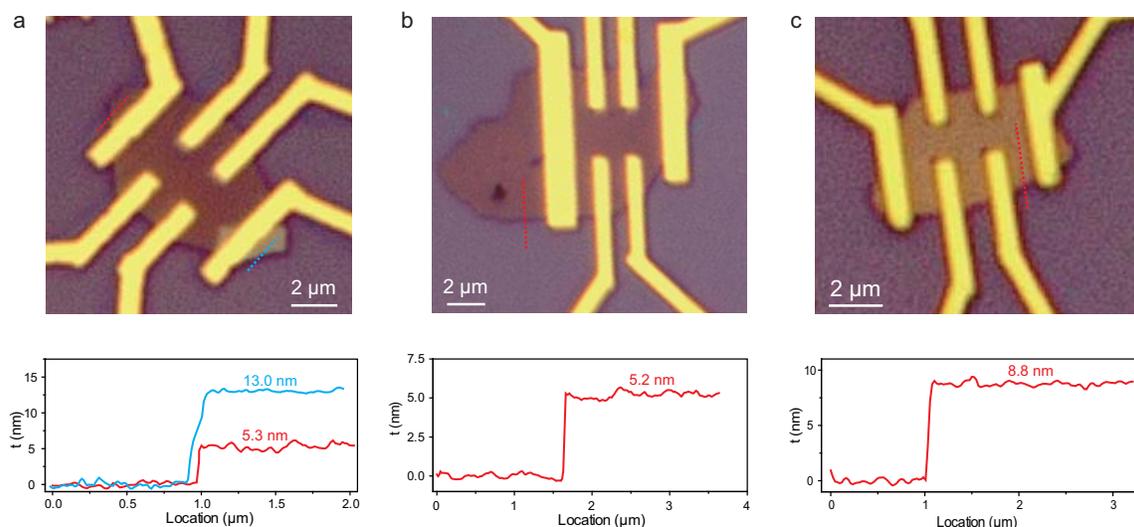
S7. Thickness of the nanoplates measured by atomic force microscopy (AFM). a,b,c, Optical microscopy images (top row) of FET devices, also shown as insets of Fig 2, Fig. 3a and Fig. 3d respectively. AFM height profiles (red solid line, bottom row) corresponding to the red dash line in the optical images, from which the thickness of the nanoplates is obtained as the averaged value. **a**, We identify an extra layer grown on the edge of the nanoplate from optical contrast, with the thickness of ~13.0 nm. It is away from the center region of the nanoplate probed by voltage electrodes, so the influence on transport measurements is negligible.
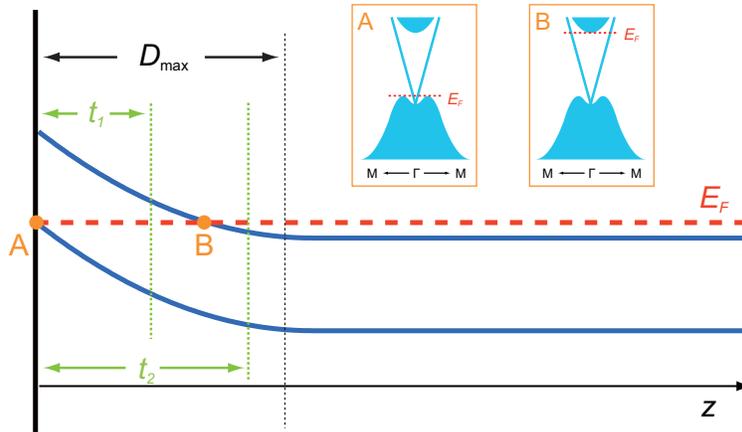
S8. Band bending due to electrostatic gating with maximum surface depletion length.

The back-gate FET device electrostatically dopes the nanoplate with additional carriers and bends the bulk band structure near the dielectric / topological insulator interface. In depletion state, such bending occurs over a surface depletion layer D. As a first order estimation, the thickness of surface depletion layer can be calculated by solving Poisson equation in the full depletion approximation to yield $D = (2\kappa \, \varepsilon_0 \, \Delta E/ \, e^2 n)^{1/2}$ [2], where κ is the dc dielectric permittivity ($\kappa \sim 56$ interpolated from the values of parent compounds; $\kappa \sim 36.5$ in Sb_2Te_3 and $\kappa \sim 75$ in Bi_2Te_3[3]) and ΔE is the shift of Fermi energy across the band bending region ($\Delta E \leq$ band gap ~ 0.2 eV). Note that the model is based on the depletion of bulk states in standard semiconductor, where the screening of topological surface states is not included to simplify the calculations.

To suppress bulk conduction, sample thickness t should be much smaller than D, so that the gate effectively modulate the charge carrier density of the entire sample. D_{max} is ~ 11 nm estimated based on the volume carrier concentration $n \sim 10^{19}$ cm^{-3}. The thicknesses of ultrathin nanoplates ($t_1 \sim 5$ nm; Fig. 3 and Fig. 4a) and slightly thicker samples ($t_2 \sim 9$ nm; Fig. 4d) are labeled in the band diagram. It is therefore not surprising to observe suppressed bulk transport in gated ultrathin samples, whereas large contribution of metallic bulk conduction is always present in thicker samples. Given the spread of carrier density, D_{max} is expected to vary slightly among nanoplates.

The aforementioned analysis is purely for an order of magnitude estimation without accounting for any non-ideality in the actual samples, such as compositional inhomogeneity and the possible presence of defect states in the bulk gap. Precise model should base on self-consistent calculations to include the finite size effect in nanostructures and the screening from 2D topological surface states. Additional knowledge of the properties at dielectric/ nanoplate interface may be required.
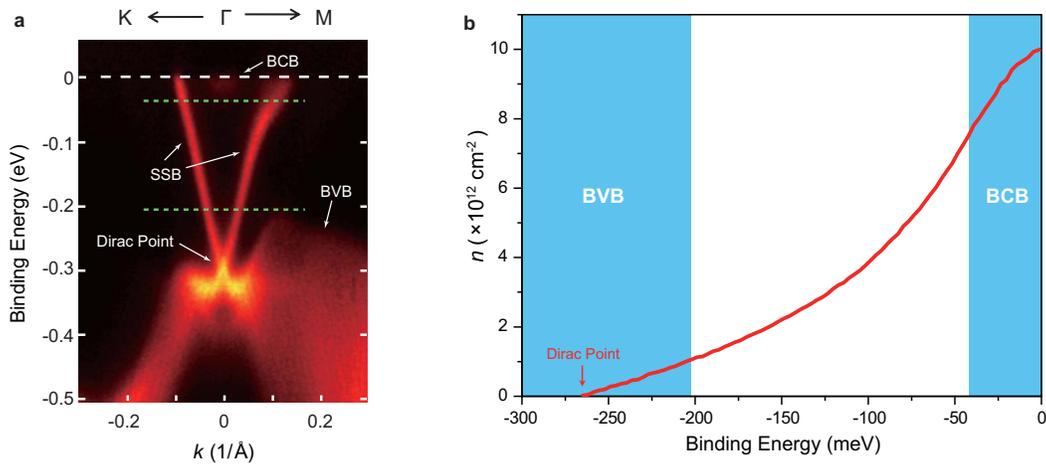
S9. Carrier concentration of topological surface states in $(Bi_xSb_{1-x})_2Te_3$ system. The surface electron density can be estimated from the surface states band (SSB) band spectrum by ARPES. We use the band structure of $(Bi_{0.75}Sb_{0.25})_2Te_3$ (shown in **a**) for such an analysis, where the bulk conduction band (BCB) and bulk valence band (BVB) are clearly observed in the measured spectrum. **b,** SSB carrier density as a function of binding energy. The Dirac point is buried in BCB and inaccessible within bulk bandgap, so finite surface carrier density ($\sim$1.0 to 7.5×10^{12} cm^{-2}) is preserved across the entire gap. It is expected that nanoplates with vanished bulk carriers would have surface carrier density between 10^{12} to 10^{13} cm^{-2} (considering the contribution from the top and bottom surfaces). The value is consistent with the lowest carrier density (outside mixed region) achieved in gated ultrathin nanoplates ($n\sim5\times10^{12}$ cm^{-2} in Fig.3 and $n\sim1.3\times10^{13}$ cm^{-2} in Fig. 4a), although the possible coexistence of bulk carriers and defect states inside the band gap cannot be excluded. Note that such an analysis is purely for an order of magnitude estimation and only applicable to crystals with relatively low Sb concentration (Surface conducting state with much lower carrier density is possible for Sb_2Te_3, where exposed Dirac point is slightly above the bulk valance band[4]).

x	$x_{EDX,1}$	$x_{EDX,2}$	$x_{EDX,3}$	$x_{EDX,4}$	$x_{EDX, average}$
0.25	0.141	0.159	0.159		0.15
0.50	0.314	0.338	0.308		0.32
0.75	0.647	0.624	0.576	0.620	0.62

S10. EDX calibration of actual composition in $(Bi_xSb_{1-x})_2Te_3$ nanoplates. The numbers in subscript is the plate number.

x	n_1	n_2	n_3	n_4	n_5	n_6	n_7	$n_{avearge}$
0	-193	-245	-277					-238
0.50	7.0	10.8	7.3	12.3	4.8	16.3	7.2	9.4
0.75	37.2	17.1	44.6	17.4				29.1
1	353	283	160	463	138			279

S11. Dependence of area carrier concenration on composition in $(Bi_xSb_{1-x})_2Te_3$ nanoplates. The electron concentration (in unit of 10^{12} cm^{-2}) is determined by Hall effect (holes shown as negative values). The numbers in subscript indicate device number.

References

[1]   Chen, J. *et al.*, Tunable surface conductivity in Bi_2Se_3 revealed in diffusive electron transport. *Phys. Rev. B* **83**, 241304 (2011).

[2]   Checkelsky, J.G., Hor, Y.S., Cava, R.J., & Ong, N.P., Bulk band gap and surface state conduction observed in voltage-tuned crystals of the topological insulator Bi_2Se_3. *Phy. Rev. Lett.* **106**, 196801 (2011).

[3]   Madelung, U.R.O. & Schulz, M. eds., Non-tetrahedrally bonded elements and binary compounds i. (Springer-Verlag, 1998).

[4]   Zhang, H. *et al.*, Topological insulators in Bi_2Se_3, Bi_2Te_3 and Sb_2Te_3 with a single Dirac cone on the surface. *Nature Phys.* **5**, 438-442 (2009).